

AVEIRO - PORTUGAL



This paper must be cited as:

Fang, M., Neto, A.N.C., Fu, L., Ferreira, R.A.S., deZeaBermudez, V., Carlos, L.D., Adv. Mater. Technol. 2021, 2100727, <https://doi.org/10.1002/admt.202100727>

A hybrid materials approach for fabricating efficient WLEDs based on di-ureasils doped with carbon dots and a europium complex

Ming Fang, Albano N. Carneiro Neto, Lianshe Fu, Rute A. S. Ferreira, Verónica de Zea Bermudez and L. D. Carlos**

Dr. M. Fang, Dr. A. N. C. Neto, Dr. L. S. Fu, Prof. R. A. S. Ferreira and Prof. L. D. Carlos

Phantom-g, CICECO – Aveiro Institute of Materials, Department of Physics, University of Aveiro, 3810-193 Aveiro, Portugal

E-mail: rferreira@ua.pt; lcarlos@ua.pt

Dr. L. S. Fu

CICECO – Aveiro Institute of Materials, Department of Chemistry, University of Aveiro

3810-193 Aveiro, Portugal

Prof. V. de Zea Bermudez

Department of Chemistry and CQ-VR, University of Trás-os-Montes e Alto Douro, 5000-801 Vila Real, Portugal

Keywords: white-light emission, visible-light-excited di-ureasil hybrids, carbon nanodots, Eu^{3+} complex, energy transfer

Abstract

White light-emitting diodes (WLEDs) revolutionized the lighting industry providing high energy efficiency and a long lifetime. The recent development of efficient ultraviolet (UV) LEDs pushed forward the development of WLEDs based on mixtures of down-shifting phosphors and the current challenges are focused on the design of sustainable light converting materials with tunable correlated color temperature (CCT) and high color rendering index (CRI). Here we report a simple route to design sustainable WLEDs with tunable and enhanced color features through the assembly of a commercial LED chip (400 nm) and flexible films of a di-ureasil hybrid comprising a mixture of a cyan component originating from amorphous carbon dots and a red one resulting from the $\text{Eu}(\text{tta})_3(\text{bpyO}_2)$ (tta^- : 2-thenoyltrifluoroacetate and bpyO_2 : 2,2'-dipyridyl-1,1'-dioxide) complex. This red emission is responsible for high CRI arising from an unprecedented efficient energy bridge between bpyO_2 and tta^- excited states mediated by the hybrid host, as modeled by theoretical calculations based on the density functional theory and intramolecular energy

transfer. WLED prototypes were fabricated with a tunable CCT from cold (5796 K) to warm (4228 K) white-light with high CRI values of 89 and 84, respectively, outperforming the state-of-the-art of UV-based WLEDs.

1. Introduction

Lanthanide (Ln^{3+})-based materials have been widely investigated for optical applications involving solid-state lighting,^[1] electronics,^[2] molecular magnetism,^[3] luminescent solar concentrators,^[4] biological imaging,^[5,6] smart labelling,^[7] The Internet of Things,^[8] and temperature sensors.^[9] One intriguing example is the contribution of Ce^{3+} for the current white light-emitting diodes (WLEDs) that revolutionized the lighting industry providing high energy efficiency and a long lifetime based on a blue-emitting LED chip coated with Ce:YAG that acts as a down-shifting phosphor.^[10] The Ce^{3+} emission occurs in the yellow spectral range and results from the partial conversion of the blue light. However, the Ce^{3+} f-d emission lacks a red spectral component challenging new materials design to ensure correlated color temperature (CCT) tuning and high color rendering index (CRI >80). In fact, the pure-color emission from the intra-4f transitions is one of the most attractive and singular features of Ln^{3+} -based materials. In particular, the intra-4f⁶ red emission of Eu^{3+} ions is an attractive candidate to enhance the high-wavelength emission in the new generation of WLEDs based on a combination of an ultraviolet (UV) LED chip and down-shifting phosphors. The replacement of the blue LED by UV-emitting ones appears as an advantage as the white light will depend only on the phosphor properties used to coat the chip.^[11]

In UV-pumped WLEDs, multilayers of phosphors with distinct color emission are generally used.^[12] The most widely investigated materials are Ln^{3+} -based organic-inorganic hybrids,^[13,14] including metal-organic frameworks (MOFs),^[15] because of their structural variety and stability. The primary blue component originates either from the organic ligands, or from Ln^{3+} ions (alone, e.g., Dy^{3+} ^[16], or combined, $\text{Eu}^{3+}/\text{Gd}^{3+}$,^[17] $\text{Eu}^{3+}/\text{Tb}^{3+}$,^[18] $\text{Eu}^{3+}/\text{Tb}^{3+}/\text{Gd}^{3+}$,^[19] and $\text{Eu}^{3+}/\text{Tb}^{3+}/\text{La}^{3+}$ ^[20]). However, WLEDs in which white light is generated from a single phase rather than by multiple emitting components (i.e., several layers comprising distinct phosphors), are the most desirable ones, as reabsorption of light is minimized, color alteration and a decrease of luminous efficiency are avoided, and the device is simplified. UV-pumped

WLED based on a single phase of a full-color-emitting phosphor would be highly advantageous, promising very small color variations, high CRI, and low cost.^[11] Presently, other requirements involving flexibility, transparency, and large-scale fabrication have also been extensively considered in white-light-emitting film fabrication, facing the new challenges of the domain of flexible and light-weight electronic devices.^[13,14,21]

To produce flexible white-light-emitting films for WLEDs, the incorporation of chromophores into organic-inorganic hybrid structures synthesized by the sol-gel method has emerged as an attractive solution to design low-cost new phosphors through an energy-saving and large-scale fabrication process.^[14,22,23] In fact, the di- and tri-urea cross-linked poly(oxyethylene) (POE)/siloxane hosts (di-ureasils^[24] and tri-ureasils^[25], respectively) demonstrated a low absorbance in the UV range ($<1 \text{ dB cm}^{-1}$)^[26] and an excellent dispersion ability that prevents the interaction of Ln^{3+} complexes with OH oscillators, reducing non-radiative deactivations^[27] and allowing the production of fine-tunable emission colors from red-to-yellow-to-green.^[13,28–33] In all the examples found, the blue component that yields white-light is provided by the intrinsic blue emission of the host^[34] or from the addition of commercial dyes^[21] or polymers.^[29] The relatively low emission quantum yield of the ureasil emission (<0.2),^[35] the difficulty to tune the emission of the dyes or polymers, and the poor photostability of their emission are important constraints motivating the search of efficient blue-emitting materials. Carbon dots (CDs) are an appropriate and attractive choice due to their fascinating properties such as straightforward synthetic routes, good water dispersibility, high stability, low toxicity, environmental friendliness, excellent biocompatibility, and tunable high-performance optical properties,^[36] and its use in UV- and blue-pumped WLEDs have emerged in the recent past.^[37–39] However, and since CDs in general still suffer from inefficient red emission and self-absorption quenching,^[40–42] WLEDs have been fabricated combining CDs and inorganic Ln-based phosphors,^[43–48] (**Table 1**). All these examples involve the coating of UV-chips with a physical mixture of CDs and the Ln^{3+} -based phosphor embedded in a polymer or a resin. This physical mixture, however, has important disadvantages such as its inhomogeneity and the poor dispersibility of the light-emitting centers in the host matrix inducing a significant self-absorption quenching, ultimately reducing the efficiency of the devices.

Herein, we propose one step beyond the generation of efficient visible-excited white-light emission in CDs-based sustainable materials and corresponding fabrication of WLEDs exploiting the aforementioned intrinsic characteristics of the d-U(600) di-ureasil hybrid matrix to incarcerate distinct and non-interacting emitting centers, amorphous CDs (aCDs) and $\text{Eu}(\text{tta})_3(\text{bpyO}_2)$, where tta^- stands for 2-thenoyltrifluoroacetate and bpyO_2 represents 2,2'-dipyridyl-1,1'-dioxide. The rationale of the complex formulation relied on the fact that, to date, significant efforts have been devoted to synthesize visible-light-excited Eu^{3+} complexes. Such compounds are mainly composed of coordinating β -diketonates and heterocycles acting as main and ancillary ligands, respectively, as depicted in Table S1, Supporting Information. 2-Thenoyltrifluoroacetone (Htta) and its derivatives are the most frequently employed β -diketonate ligands to produce efficient red emission of Eu^{3+} complexes upon UV/blue excitation.^[49–53] The fact that both light-emitting centers display analogous solubility in non-toxic solvents, such as ethanol, enabled their incorporation into the di-ureasil host featuring homogeneous film processing by the sol-gel method overcoming the well-known and aforementioned disadvantages of the physical mixture of light-converting materials. Furthermore, we demonstrate here, by means of theoretical calculations using time-dependent DFT (TD-DFT) and intramolecular energy transfer (IET), the singular and quite surprising role of the d-U(600) hybrid host in the ligand-to- Eu^{3+} energy transfer process. The hybrid host acts as an energy bridge between the bpyO_2 and the tta^- ligands permitting an efficient transfer from the latter ligand to the metal ion. This process is only possible due to the intrinsic characteristics of the di-ureasil hybrid host. It would be indeed impossible to achieve in a physical mixture. To the best of our knowledge, this is the first time that such unique effect is reported highlighting the importance of the hybrid approach to fabricate efficient WLEDs. Moreover, and as far as we know, although white-light emission has been demonstrated combining CDs and Eu^{3+} complexes (*e.g.*, $\text{Ln}(\text{dbm})_3$,^[54] $\text{Ln}=\text{Eu}$, Tb and dbm^- =dibenzoylmethanate and a Eu^{3+} complex with dbm^- and 1,10-phenanthroline ligands^[55]), no WLEDs were reported. The prototypes were fabricated by coating commercial bare LED chips (400 nm) with d-U(600) di-ureasils co-doped with aCDs and $\text{Eu}(\text{tta})_3(\text{bpyO}_2)$. The emission of the prototypes revealed tunable CCT from cold (5796 K) to

warm (4228 K) white-light with high color rendering index CRI values of 89 and 84, respectively, overwhelming the state-of-the-art of UV-based WLEDs and opening a new avenue for the fabrication of the next generation of more sustainable WLEDs made of non-toxic and low-cost materials.

2. Results and Discussion

In this thorough study of the white-light-emitting materials based on d-U(600) hybrids doped with aCDs and $\text{Eu}(\text{tta})_3(\text{bpyO}_2)$ (named hereafter dU6-aCDs/Eu) proposed here for WLEDs, it was indispensable to discuss the local structure and energy transfer mechanism after merging the chromophores into the organic-inorganic hybrid host structure. Thus, the structural and photophysical characterizations were carried out on pristine aCDs and $\text{Eu}(\text{tta})_3(\text{bpyO}_2)$, and on $\text{Eu}(\text{tta})_3(\text{bpyO}_2)$ -doped d-U(600) (dU6-Eu), aCDs-doped d-U(600) (dU6-aCDs), and aCDs- $\text{Eu}(\text{tta})_3(\text{bpyO}_2)$ -doped d-U(600) (dU6-aCDs/Eu).

2.1. Structure and photophysical properties of the $\text{Eu}(\text{tta})_3(\text{bpyO}_2)$ complex

The Fourier Transform infrared (FT-IR) spectra of the $\text{Eu}(\text{tta})_3(\text{bpyO}_2)$ complex and of the ligands are reproduced in Figure S1a, Supporting Information. The stretching vibration modes of the carbonyl (C=O) group at 1656 and 1635 cm^{-1} in free Htta (Figure S1a, Supporting Information, blue line) were shifted to 1606 and 1535 cm^{-1} in $\text{Eu}(\text{tta})_3(\text{bpyO}_2)$, respectively. This downshift confirms the coordination of the Eu^{3+} ions to the oxygen atom of the C=O groups.^[56] Moreover, the shift of the N–O stretching mode from 1254 cm^{-1} in the free bpyO₂ (Figure S1a, Supporting Information, wine line) to 1244 cm^{-1} in $\text{Eu}(\text{tta})_3(\text{bpyO}_2)$ (Figure S1a, Supporting Information, red line), is assigned to the coordination of the Eu^{3+} to the bpyO₂ ligand via the N–O groups.^[57] The weak band around 486 cm^{-1} is due to the formation of Ln^{3+} –O bonds (see arrow in Figure S1a, red line, Supporting Information).^[58]

Characteristic absorption bands are found at ~240, 290 and 340 nm for Htta and at 268 and 340 nm for $\text{Eu}(\text{tta})_3(\text{bpyO}_2)$ in the UV–visible absorption spectra of 1.0×10^{-5} M methanol solutions.^[59] The corresponding UV-visible absorption spectrum of solid-state $\text{Eu}(\text{tta})_3(\text{bpyO}_2)$ reveals a maximum absorbance centered at 398 nm, ascribed to the $\pi \rightarrow \pi^*$ transitions of the tta^- ligand, with bathochromic shift

compared to that of $\text{Eu}(\text{tta})_3(\text{bpyO}_2)$ in methanol solution (Figure S1b, Supporting Information). The relatively weak absorption peaks discerned at 464, 525, and 535 nm are attributed to ${}^7\text{F}_0 \rightarrow {}^5\text{D}_2$, ${}^7\text{F}_0 \rightarrow {}^5\text{D}_1$ and ${}^7\text{F}_1 \rightarrow {}^5\text{D}_0$ transitions of Eu^{3+} , respectively. The excitation spectrum (monitored at 612 nm) of $\text{Eu}(\text{tta})_3(\text{bpyO}_2)$ also displays a broad band in the UV/blue region, from 250 to 500 nm, and the featured intra- $4f^6$ lines (${}^7\text{F}_{0,1} \rightarrow {}^5\text{D}_2, {}^5\text{D}_1$) (Figure S1c, Supporting Information). Upon excitation at 396 nm, the $\text{Eu}(\text{tta})_3(\text{bpyO}_2)$ produces the typical $\text{Eu}^{3+} {}^5\text{D}_0 \rightarrow {}^7\text{F}_{0-4}$ transitions with emission centered at 580, 591, 612, 651, and 703 nm (Figure S1d, Supporting Information), respectively. Furthermore, the luminescence decay curve monitored around the most intense ${}^5\text{D}_0 \rightarrow {}^7\text{F}_2$ transition and upon 396 nm wavelength excitation (Figure S2, Supporting Information) exhibits a single exponential behavior with a lifetime value of 0.42 ± 0.01 ms. We notice that the complex emission is characterized by a large absolute emission quantum yield value (q) of 0.48 ± 0.05 (same wavelength excitation), becoming a promising candidate for optical applications. Both the ${}^5\text{D}_0$ lifetime and q values agree with the values reported before for the complex.^[59]

2.2 Structure and photophysical properties of the aCDs

The microwave-assisted pyrolyzed aCDs were produced via the polymerization reaction of citric acid (CA, Scheme S1a, Supporting Information) and urea (Scheme S1b, Supporting Information), followed by carbonization reactions. To investigate the impact of the molecular weight (MW) of the aCDs on their luminescence features, the as-synthesized fluorescent powders were separated into retentate and dialysate permeate fractions henceforth noted as r-aCDs (MW > 1000) and d-aCDs (MW < 1000), respectively. The d-aCDs displayed an even particle size of 0.9 ± 0.3 nm deduced from a TEM image (Figure S3, Supporting Information). The PXRD patterns are characteristic of an amorphous structure with a very weak ill-defined band appearing at around 26° for r-aCDs, assigned to the characteristic (002) diffraction peak of graphite (Figure S4a, Supporting Information). The absence of diffraction peaks from CA and urea confirms the completion of the reaction.^[60]

The mid-FT-IR spectra of CA, urea, r-aCDs, and d-aCDs are reproduced in Figure S5a, Supporting Information. In the 1800–1400 cm^{-1} interval the FT-IR spectrum of CA exhibits a characteristic pair of bands at 1742 and 1693 cm^{-1} , assigned to the asymmetric stretching vibration mode of the central and terminal carboxylic (COOH) groups, respectively, and a band at 1425 cm^{-1} , attributed to the symmetric vibration mode of the carboxylate (COO^-) groups (Figure S5b, Supporting Information, blue line).^[61–63] In the case of the FT-IR spectrum of urea, bands at 1673 and 1620 cm^{-1} , due to the Amide I vibration mode (with a major contribution of the C=O stretching, and a less marked influence of the C-N stretching, and the C-C-N deformation vibrations), and at 1587 cm^{-1} , associated with the Amide II mode (a mixed contribution of the N-H in-plane bending, the C-N stretching, and the C-C stretching vibrations), are visible in the same spectral range (Figure S5b, Supporting Information, green line).^[24,64] In the FT-IR spectra of the r-aCDs (Figure S5b, Supporting Information, orange line) and d-aCDs (Figure S5b, Supporting Information, pink line) an intense, broad and ill-resolved band envelope is found instead. This result is a further evidence of the reaction between CA and urea. The new vibration bands that emerged at 1770 and 1567 cm^{-1} are tentatively attributed to C=O groups located at the surface of the d-aCDs and r-aCDs.^[65–67] Moreover, the C–N and C=C vibration modes from the aCDs overlap with the C=O vibration modes located at 1656 and 1610 cm^{-1} (Figure S5b, Supporting Information), respectively, which also proves the typical aCDs formation.^[65–68] The absorption bands at 3430 and 3200 cm^{-1} are assigned to the O–H and N–H stretching vibration modes, respectively, whereas the bands at 3050 and 2770 cm^{-1} are attributed to stretching C–H vibration modes (Figure S5a, Supporting Information, orange and pink lines).^[69]

The UV-visible spectra of the r-aCDs and d-aCDs (Figure S4b, Supporting Information, orange and pink lines, respectively) exhibit absorption bands around 340 nm, usually attributed to the $n\text{--}\pi^*$ transition of C=C, C–N–C and C=O groups or related aromatic π systems,^[69–72] whereas the lower energy bands near 400 nm are ascribed to the convoluted surface structure of the aCDs mainly involving N doping.^[65,72] The absorption coefficient (α) of the r-aCDs is larger than that of d-aCDs being, at 395 nm, 1.10 cm^{-1} and 0.94 cm^{-1} , respectively (Figure S4b, Supporting Information). Moreover, the absorption spectrum is broader for

r-aCDs, revealing changes in the components' relative intensity, a finding which suggest that the retentate and dialysate permeate fractions impact the optical properties. The excitation wavelength-dependent emissions observed in both types of aCDs are reproduced in **Figure 1a** and **1c**, respectively. In the case of the d-aCDs the maximum emission wavelength shifted from 495 to 565 nm, with the maximum intensity being centered at 530 nm (cyan light) upon 395 nm excitation (Figure 1b). In contrast, for the r-aCDs the maximum emission wavelength shifted from 470 to 575 nm, and the maximum intensity occurred at 475 nm (blue light) upon 380 nm excitation (Figure 1d). The dependence of the maximum emission wavelength on the excitation wavelength can be ascribed to different surface states existing on aCDs, leading to distinct electronic transitions with the corresponding redshift of the emission.

In the excitation spectra of the d-aCDs and r-aCDs, the cyan emission bands are predominantly excited through a broad excitation band centered at 405 nm (Figure 1a), whereas in those of the r-aCDs the blue band emission is mainly observed under excitation at 375 nm (Figure 1b). These findings allow inferring that the featured blue range emission of the r-aCDs is primarily associated with the carbon core and/or surface states, whereas the cyan emission exhibited by the d-aCDs is essentially due to the surface states and/or molecular fluorophores related to the $n \rightarrow \pi^*$ transition of the convoluted surface structures associated with N moieties (pyrrolic-N, pyridinic-N, graphitic-N, pyridinic-N oxide, and urea-N).^[65] Besides, the r-aCDs have much lower q (0.01 ± 0.01) than the smaller d-aCDs (0.10 ± 0.01), as depicted in Table S2, Supporting Information, which reinforces the distinct origins for the emission features, as also suggested by absorption spectroscopy (Figure S4b, Supporting Information). Photographs of aqueous solutions of the d-aCDs and r-aCDs (both 1.0 mg mL^{-1}) under 365 nm and daylight irradiation are illustrated in Figure 1b and 1d, respectively. Summarizing, the d-aCDs have a more efficient cyan emission originating from carbonized polymer dots and/or carbon species carrying luminescent entities. For this reason, these were the aCDs incorporated into the di-ureasil host. Thus, in the discussion that follows whenever aCDs are mentioned, we will mean the smaller d-aCDs.

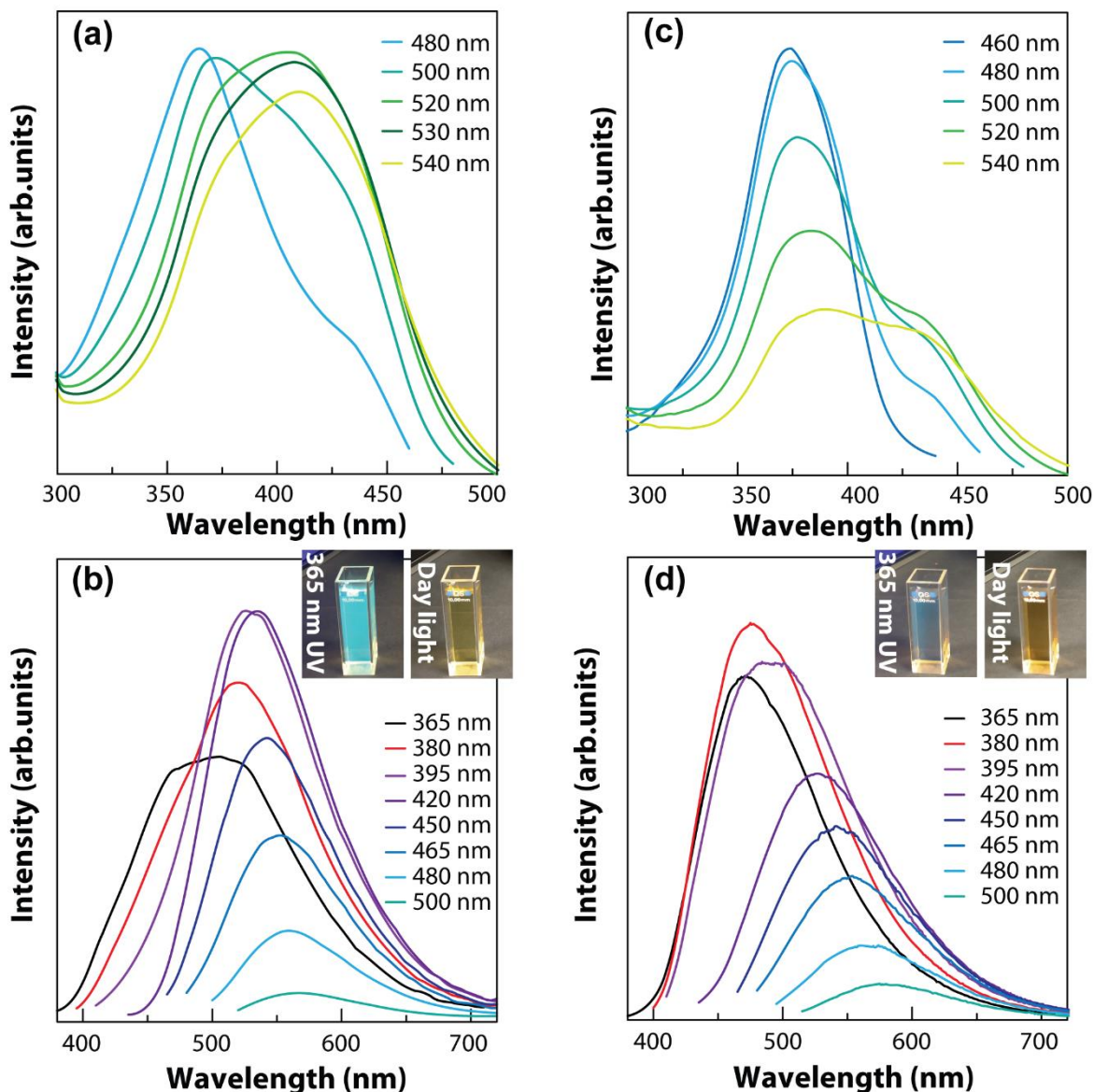


Figure 1. Excitation, a) and c), and emission spectra, b) and d), of the d-aCDs and r-aCDs aqueous solutions (0.1 mg mL⁻¹), respectively. The insets show images of the solutions under 365 nm and daylight illuminations.

2.3 Structure and photophysical properties of di-ureasils doped with aCDs and Eu(tta)₃(bpyO₂)

The PXRD patterns of dU6-aCDs, dU6-Eu, and dU6-aCDs/Eu, exhibit the typical broad peaks centered at around 20.8° and 3.0° ascribed to the presence of amorphous siliceous domains and interparticle scattering interference, respectively (Figure S6, Supporting Information).^[34] According to Bragg's formula,^[73] the characteristic structural unit distance of the amorphous siliceous domains are 4.3±0.1 Å. The interparticle scattering distance L was calculated by the Scherrer equation, $L = I \times \lambda / (A \cos \theta)$, where

$\lambda=1.54 \text{ \AA}$ is the wavelength of the Cu K α radiation, 2θ is the scattering angle, A (in radians) is the integrated area of the peak, and I is the intensity.^[74] The values found were 30.4, 27.6, and 27.6 (± 0.1) \AA for dU6-aCDs, dU6-Eu, and dU6-aCDs/Eu, respectively, in agreement with the values previously reported for the non-doped d-U(600) matrix.^[21,34]

The FT-IR spectra of d-U(600), dU6-aCDs, dU6-Eu, and dU6-aCDs/Eu (Figure S7a, Supporting Information) show broad bands centered at ~ 3540 and $\sim 3340 \text{ cm}^{-1}$, assigned to N–H and O–H stretching vibration modes, respectively. The band due to the stretching vibration of the isocyanate ($-\text{N}=\text{C}=\text{O}$) moiety of the 3- isocyanatepropyltriethoxysilane (ICPTES) precursor compound, expected at 2272 cm^{-1} , is absent in all the spectra, confirming the completion of the reaction between the $-\text{N}=\text{C}=\text{O}$ group of ICPTES and the terminal amino (NH_2) groups of the precursor ED-600 diamine. In parallel, the formation of the urea cross-links led to the growth of the characteristic Amide I and Amide II bands in the $1800\text{--}1600 \text{ cm}^{-1}$ and $1600\text{--}1500 \text{ cm}^{-1}$ spectral intervals, respectively.^[24] The Amide I and Amide II bands were decomposed into components at 1764 (F), 1720 (D3), 1686 (D2), 1664 (D1), 1640 (O), 1565, and 1515 cm^{-1} (Figure S7b, Supporting Information), where D and O stand for disordered and ordered aggregates, respectively. The integrated area fraction of the components of the Amide I band associated with “free” (non-bonded) carbonyl ($\text{C}=\text{O}$) groups (F), hydrogen-bonded $\text{C}=\text{O}$ groups of disordered POE/urea aggregates with increasing hydrogen-bonded strength (D3, D2, and D1), and hydrogen-bonded $\text{C}=\text{O}$ groups of ordered urea-urea aggregates (O),^[75] are compared (in Figure S7c, Supporting Information). Globally the band profile of d-U(600) was not dramatically perturbed by the incorporation of the guest species (Figure S7b, Supporting Information). However, close analysis of the integrated area fraction of the components resolved in the Amide I band of the four hybrid samples studied (Figure S7c, Supporting Information) demonstrates that the incorporation of aCDs and $\text{Eu}(\text{tta})_3(\text{bpyO}_2)$ into d-U(600) led to band redistribution. The most marked effect was detected, however, upon the addition of $\text{Eu}(\text{tta})_3(\text{bpyO}_2)$. Indeed, the results obtained point out that the proportion of O aggregates increased for dU6-Eu at the expense of the destruction of D2 and D3 aggregates (Figure S7c, Supporting Information, red line). In parallel, the proportion of F groups decreased.

The formation of additional O urea-urea hydrogen bonded aggregates is a fingerprint of the entrance of one (or more) C=O oxygen atoms of the urea cross-links of d-U(600) in the Eu^{3+} coordination shell, as reported previously for di-urethane cross-linked di-urethanesil analogues doped with a low concentration of $\text{Eu}(\text{tta})_3(\text{H}_2\text{O})_2$,^[76] and in close agreement with density functional theory (DFT) results and energy transfer calculations described in the next Section. In contrast, the introduction of aCDs in d-U(600) led to a marked destruction of O aggregates and to the formation of more D3 and D2 aggregates (Figure S7c, Supporting Information, blue line). In the case of dU6-aCDs/Eu (Figure S7c, Supporting Information, orange line), because of the presence of both chromophores, the participation of the urea C=O oxygen atoms in the coordination of the Eu^{3+} in $\text{Eu}(\text{tta})_3(\text{bpyO}_2)$ is, as expected, less conspicuous.

The thermogravimetric analysis (TGA) curves of $\text{Eu}(\text{tta})_3(\text{bpyO}_2)$ and dU6-Eu demonstrate that the thermal stability of the complex in a non-oxidizing atmosphere was improved upon incorporation into the hybrid, since the thermal degradation was slightly slowed down (Figure S8, Supporting Information). For $\text{Eu}(\text{tta})_3(\text{bpyO}_2)$, a major weight loss (~60%) occurred from approximately 200 to 300 °C due to the decomposition of the organic ligands (Figure S8, Supporting Information, red line). Beyond this temperature and below 800 °C, the progressive weight loss was associated with the further degradation of residues and the concomitant formation of europium oxide (Eu_2O_3) (calcd: 17.2%, found: 17.5%). For dU6-Eu, a marked weight loss (~75%) took place in the 220–400 °C temperature range, associated with the decomposition of the POE chains,^[33] followed by a further weight loss assigned to the gradual loss of the residual organic moieties (Figure S8, Supporting Information, blue line). The remaining products corresponded to silica (SiO_2) and Eu_2O_3 (calcd: 13.1%, found: 10.8%, discrepancy probably due to the residual solvents in gel). Owing to the extremely low contents of the aCDs and Eu complex in the dU6-aCDs/Eu (0.21 and 2.68 wt %, respectively), the thermal stability of dU6-aCDs/Eu is very similar to that of d-U(600) or dU6-Eu.

Figure 2a presents the UV-visible absorption spectra of free-standing films of dU6-aCDs, dU6-Eu, and dU6-aCDs/Eu, illustrated with the photograph of a flexible, transparent, yellowish color dU6-aCDs/Eu

film under daylight irradiation. The dU6-aCDs sample displays a progressive decrease of α from 51.9 to 0.03 cm⁻¹ (in the 250–600 nm range), with a 4.6 cm⁻¹ value at 400 nm (Figure 2a, blue line), whereas dU6-Eu (Figure 2a, red line) and dU6-aCDs/Eu (Figure 2a, yellow line) show larger values, $\alpha > 120.0$ cm⁻¹ in the 250–365 nm range, and subsequently with a decrease to 10.5 and 19.1 cm⁻¹ at 400 nm, respectively. The α value of non-doped d-U(600) is ~8.0 cm⁻¹ (in the 250–300 nm range), followed by a decrease to ~1.0 cm⁻¹ at 350 nm, and then further decline to less than 0.1 cm⁻¹ at 400 nm.^[21,35] Therefore, we are led to conclude that the $\alpha = 19.1$ cm⁻¹ value of dU6-aCDs/Eu at 400 nm originates from the absorption of the Eu(tta)₃(bpyO₂) and aCDs chromophores, but not from that of the hybrid host.

The emission and excitation spectra of dU6-aCDs, dU6-Eu, and dU6-aCDs/Eu are given in Figure 2b, 2c, and 2d, respectively. Additionally, the wavelength-dependent emission spectra of dU6-aCDs, dU6-Eu and dU6-aCDs/Eu are shown in Figure S9a, S9b, and S9c, Supporting Information, respectively. The emission spectrum of dU6-Eu displays a series of narrow bands (Figure 2b, red line) assigned to the typical Eu³⁺ ⁵D₀ → ⁷F₀₋₄ transitions with q values of 0.12 ± 0.01 and 0.05 ± 0.01 under 395 and 410 nm irradiations (Table S3, Supporting Information), respectively. The dU6-aCDs produce a broadband emission in the blue-green range centered at 500 nm (Figure 2c, blue line) and an excitation wavelength-dependent emission feature (Figure S9a, Supporting Information), analogous to the pure r-aCDs in distilled water (Figure 1d). The maximum emission wavelength displays a solvatochromic blue shift with respect to the aqueous solution (Figure 1d), in the entire excitation wavelength range. The less polar surrounding environment in d-U(600) relative to that found in water results in a larger energy gap between the excited and ground states of aCDs and, consequently, leading to a shorter wavelength of recombination.^[77] The q for the d-aCDs is markedly boosted from 0.10 ± 0.01 to 0.39 ± 0.04 upon incorporation into d-U(600) (Table S2 and S3, Supporting Information), which is attributed to the encapsulating effect exerted by the di-ureasil host, as already noticed in aCDs dispersed in poly(vinylpyrrolidone) ($q = 0.39$)^[77] or polyhedral oligomeric silsesquioxanes ($q = 0.60$).^[78]

To take advantage of the possibility of simultaneously exciting the Eu^{3+} -based complex and the aCDs with visible radiation, a di-ureasil sample including both guest species was prepared (dU6-aCDs/Eu). The combination of the broad emission band (blue–green) centered at 500 nm and the red emission yielded white-light emission upon 400 nm excitation (Figure 2d, yellow line), with $q=0.15\pm0.02$ and 0.14 ± 0.01 under 395 and 410 nm excitation, respectively. The wavelength-dependent emission spectra of dU6-aCDs/Eu are shown in Figure S9c, Supporting Information, and the corresponding color coordinates are presented in Figure S10, Supporting Information. The emission was fine-tuned, shifting from pure red (0.659, 0.329) at 365 nm to cyan (0.254, 0.457) at 420 nm excitation, crossing the white region (0.304, 0.411) at excitation around 400 nm. The latter result is very promising for the fabrication of a WLED based on a commercial low-energy emitting LED chip (Figure S11, Supporting Information).

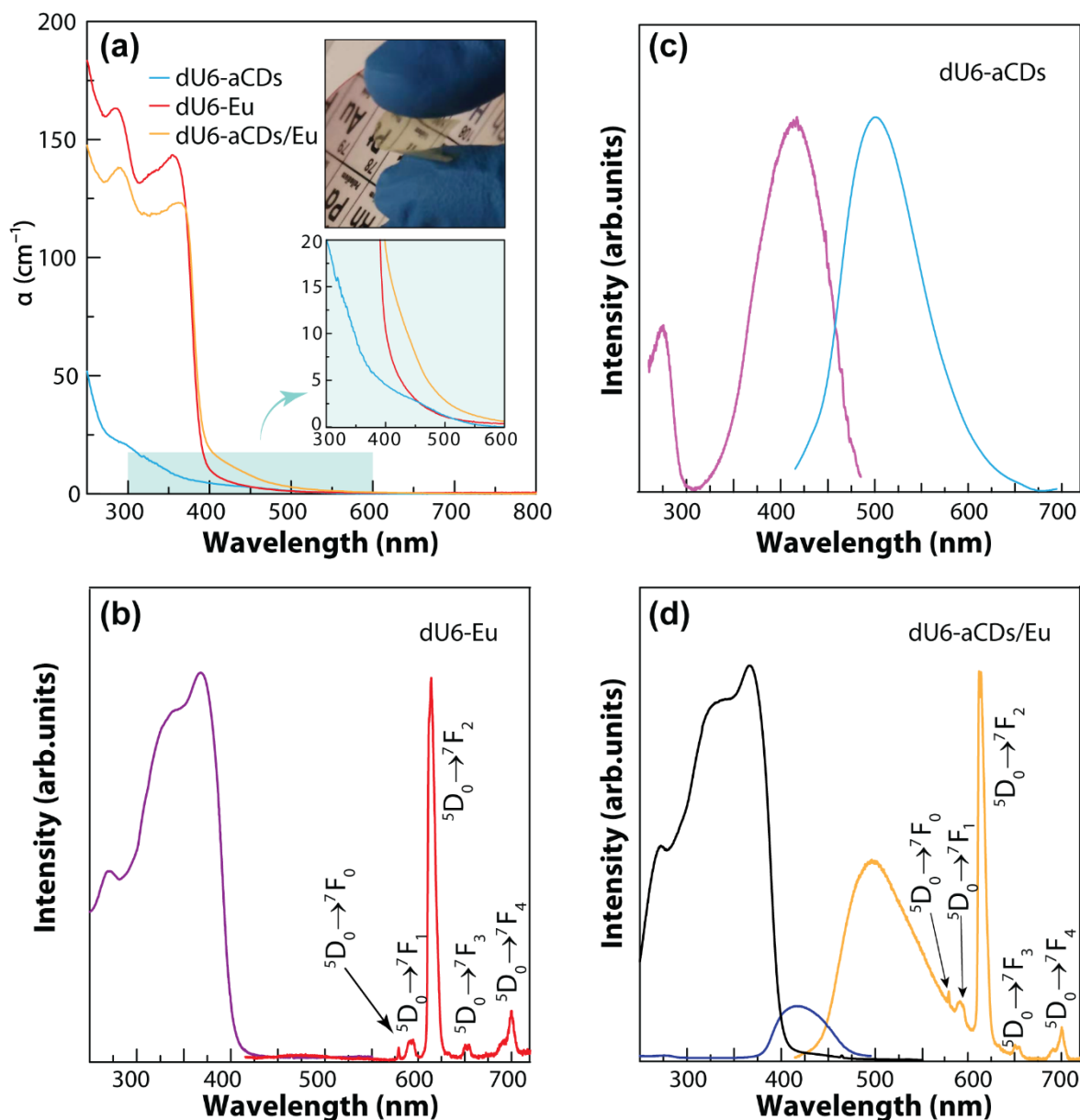


Figure 2. a) UV–visible absorption spectra of dU6-aCDs, dU6-Eu, and dU6-aCDs/Eu. Emission and excitation spectra of b) dU6-Eu (excited at 400 nm and monitored at 614 nm), c) dU6-aCDs (excited at 400 nm and monitored at 500 nm), and d) dU6-aCDs/Eu (excited at 400 nm and monitored at 614 or 510 nm). The inset shows a photograph of a flexible dU6-aCDs/Eu film.

The Eu^{3+} local coordination in the doped di-ureasils was discussed based on the comparison between the emission spectra of dU6-Eu and dU6-aCDs/Eu (Figure 2b and 2d and Figure S12, Supporting Information) with that of $\text{Eu}(\text{tta})_3(\text{bpyO}_2)$ (Figure S1d, Supporting Information). The detection of a single (non-degenerated) $^5\text{D}_0 \rightarrow ^7\text{F}_0$ peak, the Stark splitting of the $^5\text{D}_0 \rightarrow ^7\text{F}_{1,2}$ transition in 3 and 5 components, respectively, and the high relative intensity of the hypersensitive $^5\text{D}_0 \rightarrow ^7\text{F}_2$ transition indicate that the Eu^{3+}

ions occupy a single low-symmetry point group without an inversion center in all the samples. This is exactly the conclusion of the single crystal data of $\text{Eu}(\text{tta})_3(\text{bpyO}_2)$.^[59] Nevertheless, comparison of the energy, full-width-at-half-maximum (fwhm) and relative intensity of the $^5\text{D}_0 \rightarrow ^7\text{F}_{0-4}$ transitions in the pristine complex with those in the hybrids, evidences significant changes (Figure 2c and 2d, and Figure S1d, Supporting Information). Such differences induced by the $\text{Eu}(\text{tta})_3(\text{bpyO}_2)$ incorporation into the d-U(600) matrix are well illustrated by the blue-shift (from 17245 ± 1 to $17265 \pm 1 \text{ cm}^{-1}$) and the broadening (from 20 ± 1 to $56 \pm 1 \text{ cm}^{-1}$) of the $^5\text{D}_0 \rightarrow ^7\text{F}_0$ transition observed in dU6-Eu and dU6-aCDs/Eu relatively to the values observed in the pristine complex. These differences are ascribed to an effective interaction between the complex and the d-U(600) host resulting from the inclusion of the oxygen atoms of the carbonyl groups of the urea cross-links in the Eu^{3+} first coordination shell, as previously noticed in analogous doped di-ureasils.^[76,79] This is also inferred from the changes in the excitation spectra (Figure 2b and 2d, and Figure S1c, Supporting Information) and the significant decrease in the q values, 0.48 ± 0.05 in $\text{Eu}(\text{tta})_3(\text{bpyO}_2)$ and 0.12 ± 0.01 and 0.15 ± 0.02 in dU6-Eu and dU6-aCDs/Eu, respectively (Table S4, Supporting Information). All these results are compatible with the coordination of the oxygen atoms of the carbonyl groups to the Eu^{3+} ions in the hybrids, as the aforementioned FT-IR results suggest, and as the DFT results and ligand-to-metal energy transfer calculations described in the next section will demonstrate. Moreover, there are no significant differences between the Eu^{3+} emission in dU6-Eu and dU6-aCDs/Eu, as indicated by the similarity between their emission spectra (same energy and fwhm for the $^5\text{D}_0 \rightarrow ^7\text{F}_0$ peak and analogous Stark splitting, energy and fwhm of the $^5\text{D}_0 \rightarrow ^7\text{F}_{1-2}$ transitions, Figure S12, Supporting Information). This points out a negligible IET between the aCDs and $\text{Eu}(\text{tta})_3(\text{bpyO}_2)$ emitting centers in the hybrids, a conclusion further reinforced by the similar $^5\text{D}_0$ lifetimes detected in dU6-Eu and dU6-aCDs/Eu (Figure S13 and Table S4, Supporting Information).

2.4 Theoretical results and remarks

In principle, the energy transfer inside the multi-chromophores-doped d-U(600) hybrids is incredibly complicated due to the potential energy transfer among Eu^{3+} ions, ligands, aCDs, and the d-U(600) host. However, as discussed in the previous section, there is no energy migration between the aCDs and the $\text{Eu}(\text{tta})_3(\text{bpyO}_2)$ complex. Thus, the energy transfer process for the dU6-aCDs/Eu can be simplified in the dU6-Eu system. The geometry optimization (Figure S14 and S15, Supporting Information) using DFT confirms that a carbonyl group of the urea bridges is coordinated to the Eu^{3+} (Figure S16, Supporting Information), corroborating with the FTIR and photoluminescence results (see above) and also observed previously.^[76,79]

Based on DFT and intramolecular energy transfer (IET) calculations (see Supporting Information), an energy levels diagram was constructed (**Figure 3**). The essential rates involved in the dU6-Eu system are labeled with numbers from 1 to 8 (Table S6, Supporting Information, shows all individual IET pathways). Time-dependent DFT (TD-DFT) calculations provided the molecular orbitals (MOs) compositions involved in the S_1 and T_1 states (Figure S15, Supporting Information). Interestingly, the excited state S_1 is located at the bpyO_2 ligand, whereas the T_1 state is spread among the three tta^- ligands.

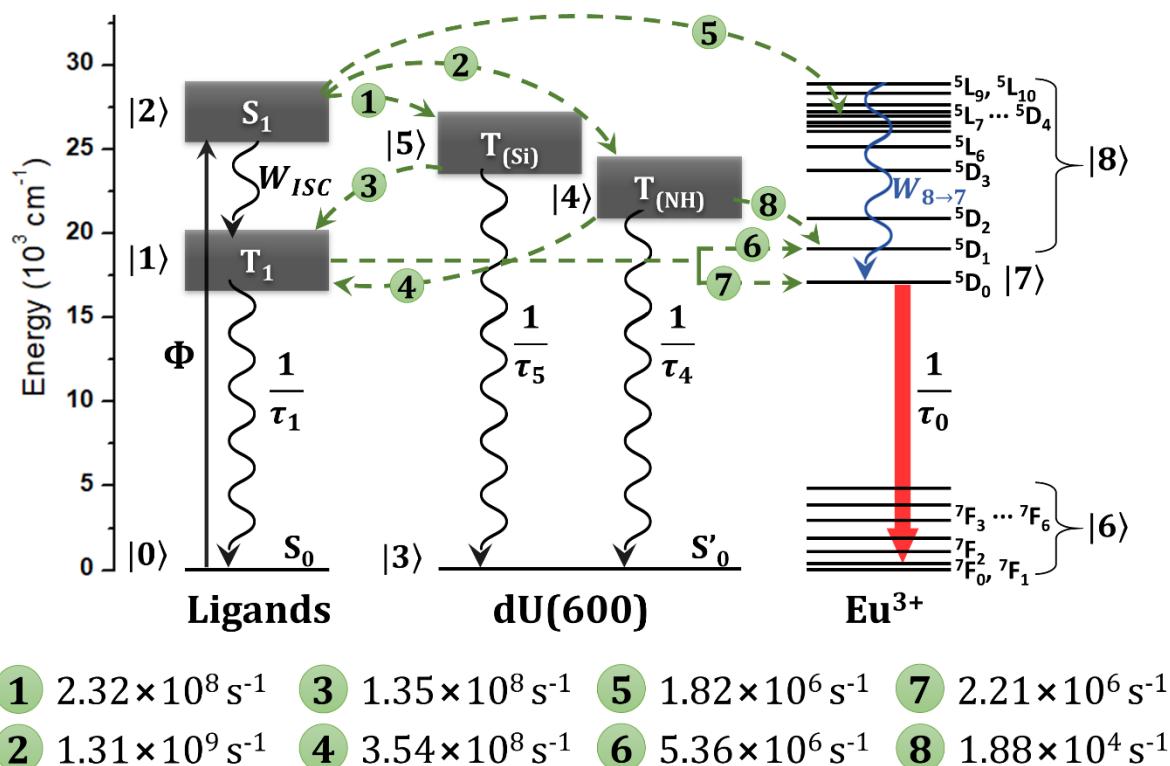


Figure 3. Schematic energy level diagram in the independent systems model (ligands, d-U(600), and Eu^{3+} ion). The most effective energy route is $\text{S}_1 \rightarrow \text{T}_{(\text{Si})}(1)/\text{T}_{(\text{NH})} \rightarrow \text{T}_1(4) \rightarrow \text{Eu}^{3+}$ (${}^7\text{F}_0 \rightarrow {}^5\text{D}_1$ (6) and ${}^7\text{F}_1 \rightarrow {}^5\text{D}_0$ (7)). For the pursuit of clarification, only the relevant rates are displayed. More details on all rates involved are given in Table S6, Supporting Information. The d-U(600) singlet state was not included because its energetic position is above $40,000 \text{ cm}^{-1}$ [80] and, consequently, it does not have energy resonant conditions to be a good acceptor, even from the S_1 maximum absorption band (ca. $30,000 \text{ cm}^{-1}$). See the Supporting Information for more details on the rates in the diagram.

The kinetics was solved using an appropriated system of equation rates (ordinary differential equations (ODEs), Equations S18 to S24). The respective population fractions, in the steady-state regime, of the ${}^5\text{D}_0$, T_1 , and ground levels, are 0.052, 1.638×10^{-5} , and 0.948, respectively (Figure S17, Supporting Information). The other S_1 , $\text{T}_{(\text{Si})}$, and $\text{T}_{(\text{NH})}$ levels, as well as the Eu^{3+} states above the ${}^5\text{D}_0$ have a negligible population ($<10^{-7}$).

The total radiative rate ($A_{\text{rad}}=881 \text{ s}^{-1}$) of the ${}^5\text{D}_0$ was extracted from the experimental emission spectrum of the dU6-aCDs/Eu sample (Figure S18, Supporting Information), which is given by $A_{\text{rad}} = \sum_j A_{0 \rightarrow j}$, where $A_{0 \rightarrow j}$ (Equation S27) is the radiative rate of ${}^5\text{D}_0 \rightarrow {}^7\text{F}_j$ (J from 0 to 4) emissions. Using the values obtained for dU6-aCDs/Eu excited at 380 nm, a theoretical value of $q=0.25$ at 380 nm was deduced,

corroborating the experimental value, 0.26 ± 0.03 , Table S3, Supporting Information. Behind this good theory-experiment agreement, the interaction of the hybrid moieties with the S_1 state plays a special role in the overall energy transfer process, which is consequently, manifested in the q values. A satisfactory explanation is that a relatively high fluorescence rate of the $S_1\rightarrow S_0$, normally in the order of nanoseconds, and a considerable large energy gap between S_1 and T_1 ($\sim 6500\text{ cm}^{-1}$) may not favor the intersystem crossing. In the absence of interaction with the hybrid host, there are no energy interchanges between the bpyO₂ ligand (S_1) and the d-U(600) moieties ($T_{(Si)}$ and $T_{(NH)}$), pathways **1** and **3** in Table S6, Supporting Information. This promotes a fast depopulation of the S_1 level via fluorescence decay $S_1\rightarrow S_0$, blocking the relatively slower energy transfer via $S_1\rightarrow T_1$ or $S_1\rightarrow Eu^{3+}$, once these rates, in the present case, are 1000 times smaller than that of $S_1\rightarrow S_0$. This barrier is bypassed by the hybrid that serves as an energy bridge between the S_1 and T_1 levels. In other words, there is a synergy interaction in which the d-U(600) acts as a receptor of energy from bpyO₂ ligand, delivering it then to the tta⁻ ligands, which in turn transfer the energy more effectively to the Eu^{3+} ion. To illustrate the synergy situation just described, Figure S19, Supporting Information (and the related discussions around) represents the population analysis in the absence of d-U(600) energy interaction. The population of the emitting level 5D_0 drops by a factor of 213 (from 0.054 to 2.537×10^{-4}) leading to a very low absolute emission quantum yield value, $q\sim 0.0012$.

2.5. WLED prototypes

To evaluate the white-light emission of dU6-aCDs/Eu, four WLEDs (named **W1**, **W2**, **W3** and **W4**) coated with increasing dU6-aCDs/Eu gel amounts (up to $\sim 30\text{ mg}$) were fabricated using commercial blue (400 nm) LED chips. **Figure 4a** and **4b** display the photos of prototype **W4** under daylight and upon a driving current of 2 mA. The emission color coordinates in the CIE 1931 chromaticity diagram shift from (0.321, 0.367) cold white lighting with CCT of 5949 K to (0.390, 0.455) warm white lighting with CCT of 4228 K (**Table 1**), along with a maximum q value of 0.23 ± 0.02 (prototype **W1**). The WLED prototypes meet the requirements for indoor lighting ($CRI>85$ and $CCT<4500\text{ K}$)^[81] with $CRI=84.2$ and $CCT=4228$

K (prototype **W4**). The slight decrease in q suggests the self-absorption of aCDs and the scattering of the emitted photons induced by the increasing thickness.^[82] Nonetheless, we notice that the thicker the films, the larger is the absorption, reaching 98% for prototype **W4** (Table S7, Supporting Information). The emission spectra of the WLED prototype were recorded under continuous operation for 300 min, revealing an analogous fade of the contribution of the $\text{Eu}(\text{tta})_3(\text{bpyO}_2)$ complex and the d-aCDs. Under continuous operation, the WLED prototype reveals a decrease of around 30% of its initial intensity (Figure S20 Supporting Information). This aspect was quantified through the CIE (x,y) emission color coordinates measured immediately after the WLED was turned on ($t=0$) and after 300 min of operation. In both cases, the (x,y) colour coordinates lie in the warm white region changing from (0.42;0.42), $t=0$, to (0.46,0.42), $t=300$ min. The slight deviation toward the red suggests that CDs present a larger contribution to photodegradation.

The comparison between LEDs' performance is typically characterized by the luminous efficacy (LE, lm W^{-1}), which accounts for the ratio between the luminous flux (lm) and the electric power (W). We should note, however, that a direct comparison of these values between distinct WLEDs must be taken with caution as they depend on the wall-plug efficiency of the UV-pumped LED and on the device geometry. In particular, the comparison between WLED prototypes based on blue- or UV-LED chips is not accurate as the later ones consume lower electrical power and, therefore, larger LE is expected. Moreover, the rationale behind white light generation is distinct. While in the case of UV-pumped LEDs, white light is only generated from the down-shifting phosphors, in the case of blue-pumping, white light results from the sum of the blue light from the electroluminescent pumping chip and the phosphor emission. In this latter case, the luminous flux also accounts for photons arising from the blue LED chip electroluminescence and the phosphor emission. This is not the case with UV-pumped WLEDs in which the luminous flux only weighs the phosphor contribution. Therefore, an accurate comparison with the state-of-the-art must be restricted to include WLEDs based solely on analogous UV chips, in which white light results from the UV-down shifting phosphors. Examples including single-component white light-emitting materials based on a single

layer so far are rather limited (Table 1). As far as we know, only one example reports the fabrication of WLEDs based on UV chips and a single layer based on the combination of CDs and Ln-based phosphors.^[48] Despite lower LE is found for **W1-W4** prototypes, lower CCT and high CRI were attained, in line with the need for the new generation of WLEDs. Moreover, the performance of **W3** is comparable to that of some state-of-the-art WLEDs based solely in CDs or in the combination of CDs and Ln-based phosphors (Table 1).

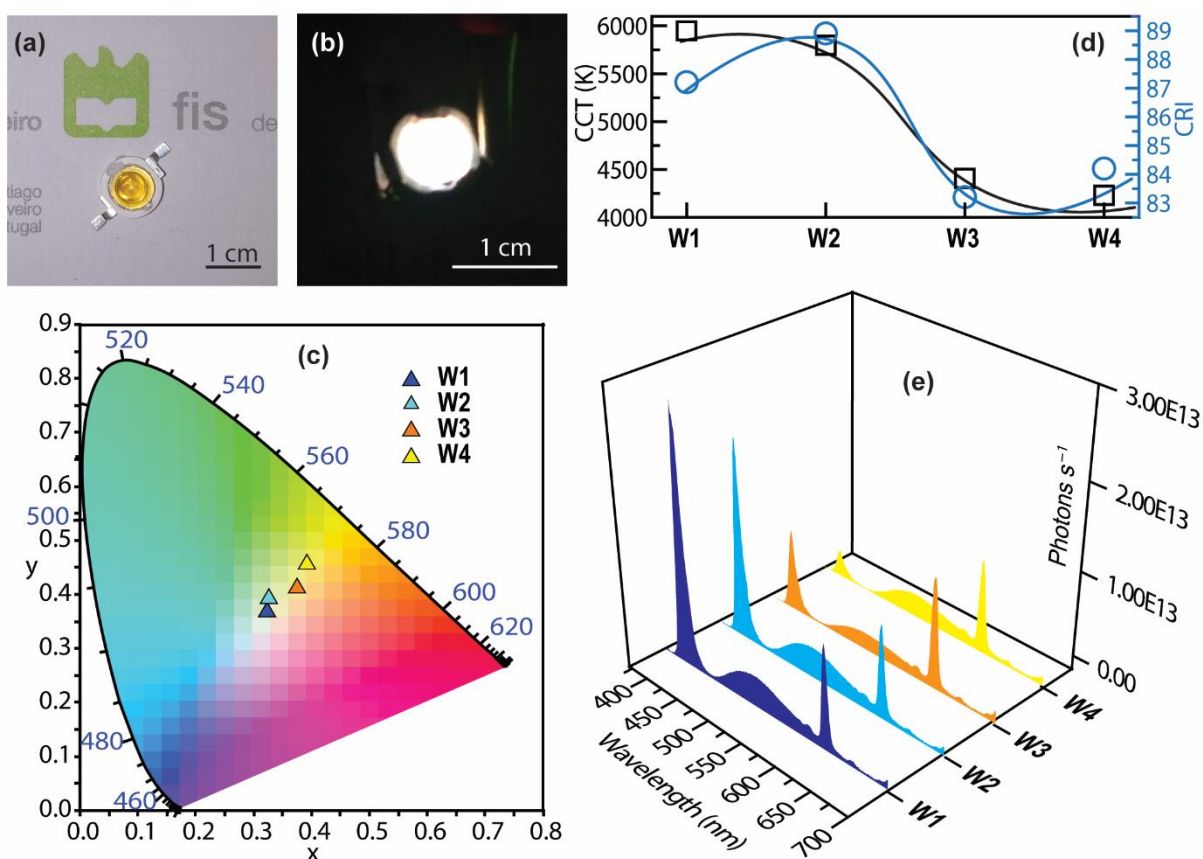


Figure 4. Photos of a dU6-aCDs/Eu-LED under a) daylight irradiation and b) upon a driving current of 2 mA in the dark; c) CIE 1931 chromaticity diagram showing the CIE (x,y) emission color coordinates of dU6-aCDs/Eu-coated WLEDs **W1**, **W2**, **W3**, and **W4**; d) relationship between CCT and CRI for the WLEDs **W1**, **W2**, **W3**, and **W4** (the lines are visual guides); e) photon flux of the WLEDs **W1**, **W2**, **W3**, and **W4**, showing the photoluminescence of the aCDs and Eu³⁺ ions and the electroluminescence of the blue chip (cf. Figure S11, Supporting Information).

Table 1. CIE color coordinates, CRI, CCT (K), and LE (lm·W⁻¹) values of UV (254-400 nm) and blue (405 nm) downshifting WLEDs based on the combination of CDs and Ln-based phosphors. Illustrative

examples of single-layer devices fabricated only with CDs are also listed for comparison. The LED commercial chip maximum peak wavelength (nm) is also indicated.

Phosphor	Wavelength	CIE color coordinates	CRI/CCT	LE	Reference
Single layer					
dU6-aCDs/Eu (W1)	400	(0.321,0.367)	87/5949	11.2	This work
dU6-aCDs/Eu (W2)	400	(0.324,0.390)	89/5796	11.2	This work
dU6-aCDs/Eu (W3)	400	(0.373,0.412)	83/4406	13.2	This work
dU6-aCDs/Eu (W4)	400	(0.390,0.455)	84/4228	9.5	This work
CDs/YAG:Ce ³⁺ a)	360	(0.296,0.311)	75/7342	19.9	[48]
Multi-layers					
CDs/Sr ₂ Si ₅ N ₈ :Eu ²⁺	375	(0.30,0.33)	94/7283	—	[47]
CDs/SrSi ₂ O ₂ N ₂ :Eu ²⁺ and CDs/Sr ₂ Si ₅ N ₈ :Eu ²⁺	360	(0.33,0.37)	95/5447	—	[46]
CDs/CaAlSiN ₃ :Eu ²⁺	395	(0.382,0.391)	87/3863	17.2	[45]
CDs/LaF ₃ :Ce ³⁺ /Tb ³⁺ /Sm ³⁺	254	(0.33,0.32)	—	8.7	[43]
CDs/CaAlSiN ₃ :Eu ²⁺	395	(0.371,0.397)	86/4340	31.3	[44]
Single-layer					
AC-CDs	400	(0.33,0.33)	92/—	30.5	[83]
CDs@PS	380	(0.35,0.36)	93/4075	14.8	[84]
Cl-GQDs	360	(0.3254,0.3445)	88/5653	5.1	[85]
SW-CPDs	370	(0.268,0.346)	85/8756	18.7	[37]

a) Physical mixture of S, N co-doped graphene quantum dots and YAG:Ce³⁺ embedded into polyvinyl alcohol (PVA); AC-CDs=N-doped multiple-core@shell-structured CDs; PS=polystyrene; Cl-GQDs=chlorine-doped graphene quantum dots; SW-CPDs=white-light-emissive carbonized polymer dots.

3. Conclusion

In summary, flexible and transparent di-urea cross linked POE/silica di-ureasil hybrid films doped with Eu(tta)₃(bpyO₂) and aCDs were synthesized by the sol-gel method with enhanced thermal-stability and efficient white-light emission upon visible light (400 nm) excitation, based on the merits of ligand-induced large Stokes shift of red emission from the Eu³⁺ complex and small Stokes shift of cyan emission from the aCDs. Based on experimental evidence, the intermolecular energy transfer between aCDs and

Eu(tta)₃(bpyO₂) is negligible. Theoretical calculations on the intramolecular energy transfer regarding the red emission were performed showing that the hybrid host has an important and unprecedented role in the ligands-to-Eu³⁺ energy transfer process, reported and described in detail here for the first time. The host serves as an energy bridge between the bpyO₂ (related to the S₁ state) and tta⁻ (related to the T₁ state) ligands, due to faster energy transfer rates from the bpyO₂ to the host (T_(Si) and T_(NH) energy levels) in comparison to the usual W_{ISC} rates. Those rates even in better energy conditions with ΔE_{S-T} (S₁ and T₁ energy difference) around 2000 cm⁻¹ were estimated to be in the order of W_{ISC}~10⁷ s⁻¹ for organic compounds.^[86] However, in our case, the ΔE_{S-T}=6500 cm⁻¹ is much higher and the W_{ISC} (considered to be 10⁶ s⁻¹) still is 1500 times less than the energy transfer rates from the bpyO₂ to the host and 480 times from the host to the tta⁻ ligand. This unique effect, never reported before, is only possible due to the intrinsic characteristics of the di-ureasil host, highlighting the pivotal interest of the hybrid approach to produce efficient WLEDs. The emission of the prototypes fabricated by coating commercial bare LED chips (400 nm) with d-U(600) di-ureasils co-doped with aCDs and Eu(tta)₃(bpyO₂) revealed tunable CCT from cold (5796 K) to warm (4228 K) white-light with high color rendering index CRI values of 89 and 84, respectively, and significant *q* (0.15–0.23) overwhelming the state-of-the-art UV-downshifting sustainable phosphors used in WLEDs. The present organic-inorganic flexible and transparent hybrid films show versatile shaping and patterning, facile tunable white-light, energy-saving feature, cheap price, and large-scale fabrication feasibility which hold a promising future for weight-light wearable electronic devices.

4. Experimental section

Materials: Jeffamine[®] ED-600 polyetheramine (ED-600, Huntsman, where 600 denotes the average polymer molecular weight), ICPTES (95%, Aldrich), tetrahydrofuran (THF 99%, Sigma-Aldrich), CA (99%, Sigma-Aldrich), urea (99%, Sigma-Aldrich), Htta (99%, Sigma-Aldrich), bpyO₂ (98%, Sigma-Aldrich), europium chloride hexahydrate (EuCl₃·6H₂O, 99.9%, Sigma-Aldrich), absolute ethanol (EtOH, 99.8%, Sigma-Aldrich), methanol (MeOH, 99.8%, Sigma-Aldrich), hydrochloride acid (HCl, 99.8%,

Sigma-Aldrich) and sodium hydroxide (NaOH, 99.8%, Sigma-Aldrich) were utilized without purification. Distilled water was used throughout the experiment.

Synthesis of aCDs: The aCDs were synthesized according to the procedure reported in the literature.^[66,67] Typically, 2.0 g of CA and 2.0 g of urea were dissolved in 20 mL of distilled water in a beaker by ultrasonic bath for 20 min. The solution was then treated in a microwave oven for 5 min at 750 W. During microwave irradiation, water was first evaporated. The remaining viscous white syrup was gradually transformed into a dried brown-black foamed membrane accompanied with sparkle, which ultimately turned total black. The black product was dissolved in water after 20 min in an ultrasonic bath. The resulting solution was then filtered twice through filter paper (VWR, 2–3 μm particle retention). The filtrate was placed in a dialysis membrane (1 kDa molecular weight cut-off (MWCO), Fisher Scientific Lda, Portugal), sealed, and then immersed in distilled water. For better separation of the aCDs, the distilled water was changed 5 times during 24 h. As noted above, the aCDs in the retentate and dialysate permeate fractions were denoted as r-aCDs (MW>1000) and d-aCDs (MW<1000), respectively.

Synthesis of d-U(600) doped with aCDs: The non-hydrolyzed di-ureasil precursor (di-ureapropyltriethoxysilane, d-UPTES(600)) was prepared according to a procedure reported elsewhere^[24] (Supporting Information). Typically, 0.5 g of d-UPTES(600) was mixed with 1 mL of EtOH under stirring for 20 min at room temperature. In parallel, a solution composed of 49.4 μL of 0.01 M HCl and 200 μL of d-aCDs (4.3 mg mL^{-1} aqueous solution) was added dropwise to the above ethanolic solution of d-UPTES(600) in sequence, followed by 2 h of stirring at room temperature. The resulting solution was transferred to an oven at 50 $^{\circ}\text{C}$ and the resulting free-standing film was dried for more than 48 h. The as-prepared sample was labeled dU6-aCDs.

Synthesis of $\text{Eu}(\text{tta})_3(\text{bpyO}_2)$: The $\text{Eu}(\text{tta})_3(\text{bpyO}_2)$ complex responsible for the red emission component of WLEDs was synthesized and characterized in a previous work.^[59]

Synthesis of d-U(600) doped with $\text{Eu}(\text{tta})_3(\text{bpyO}_2)$: Typically, 0.5 g of d-UPTES(600) was mixed with 1 mL of EtOH under stirring for 20 min, followed by the addition of 11.0 mg of $\text{Eu}(\text{tta})_3(\text{bpyO}_2)$ in a

solution composed of 1.0 mL of EtOH and 49.4 μL of the 0.01 M HCl solution. The resulting solution was stirred at room temperature and then transferred to an oven at 50 $^{\circ}\text{C}$. The as-produced di-ureasil doped with $\text{Eu}(\text{tta})_3(\text{bpyO}_2)$, designated as dU6-Eu, was dried at 50 $^{\circ}\text{C}$ for more than 48 h.

Synthesis of d-U(600) co-doped with the $\text{Eu}(\text{tta})_3(\text{bpyO}_2)$ complex and d-aCDs: 0.5 g of d-UPTES(600) was mixed with 1 mL of EtOH under stirring for 20 min, followed by the addition of 11.0 mg of $\text{Eu}(\text{tta})_3(\text{bpyO}_2)$ in a solution composed of 1.0 mL of EtOH, 200 μL of an aqueous solution of d-aCDs (4.3 mg mL^{-1}) and 49.4 μL of the 0.01 M HCl solution. The resulting mixture was dried at 50 $^{\circ}\text{C}$ for more than 48 h to form the co-doped d-U(600), named as dU6-aCDs/Eu. The contents of aCDs and $\text{Eu}(\text{tta})_3(\text{bpyO}_2)$ in the dU6-aCDs/Eu hybrid were calculated to be 0.21 and 2.68 wt %, respectively.

Fabrication of the WLED prototypes: The WLEDs were fabricated using a remote phosphor configuration strategy.^[87] Typically, volumes of 10, 15, 25, and 35 μL of the dU6-aCDs/Eu sol were cast separately on the removable houses (or caps) of the LED chips (400 nm, $\text{EQE}=21.9\%$, Shenzhen Looking Long Technology Co., Ltd., China,) and then moved to an oven at 50 $^{\circ}\text{C}$ for more than 48 h. The as-formed gels (which stayed in the caps and, thus, not in direct contact with the chips) were assembled back to the LED chips to afford 4 distinct WLEDs (labelled as **W1**, **W2**, **W3** and **W4**). The thickness of the dU6-aCDs/Eu hybrid layers in **W1**, **W2**, **W3** and **W4** were 0.005, 0.008, 0.016, and 0.021 (± 0.005) mm, respectively (as measured by a Vernier Caliper).

Characterization: UV-visible absorption spectra were obtained with a resolution of 1.0 nm using a dual-beam spectrometer Lambda 950 (PerkinElmer). Because of the unknown concentration of emitting centers in the suspensions (aCDs) and hybrid samples (aCDs and Eu^{3+} ions), the absorption coefficient, $\alpha = \varepsilon c$, was considered constant in the aCDs aqueous solution and in the hybrid materials when using the Beer-Lambert law:

$$A = \log_{10} \frac{I_0}{I} = \varepsilon c l = \alpha l \quad (1)$$

where A is the absorbance, I_0 and I the incident and transmitted light, respectively, ε is the molar attenuation coefficient, c is the concentration of the attenuating absorbing species, and l is the light optical path (film thickness in cm).

Powder X-ray diffraction (PXRD) patterns were measured using a Panalytical Empyrean Diffractometer under the exposure of $\text{CuK}\alpha$ radiation (1.54 \AA) between 2θ from 3.5 to 90.0° .

Fourier transform infrared (FT-IR) spectra were recorded from 4000 to 400 cm^{-1} by averaging 512 scans at a spectral resolution of 1 cm^{-1} using a MATTSON 700 FT-IR spectrometer. The integrated areas of the components of the Amide I and Amide II bands were calculated by spectral deconvolution in the $1900\text{--}1418 \text{ cm}^{-1}$ range using the PeakFit® software and Gaussian band shapes.

Transmission electron microscopy (TEM) images were obtained using a Hitachi H9000 microscope.

The photoluminescence spectra and the photostability (under excitation at 400 nm) were recorded with a modular double grating excitation spectrofluorimeter with a TRIAX 320 emission monochromator (Fluorolog-3, Horiba Scientific) coupled to a R928 Hamamatsu photomultiplier, using a front face acquisition mode. The excitation source was a 450 W Xe arc lamp. The emission spectra were corrected for detection and optical spectral response of the spectrofluorimeter and the excitation spectra were corrected for the spectral distribution of the lamp intensity using a photodiode reference detector. The time-resolved measurements were done with the setup described for the luminescence spectra using a pulsed Xe-Hg lamp ($6 \text{ }\mu\text{s}$ pulse at half-width and $20\text{--}30 \text{ }\mu\text{s}$ tail).

The emission quantum yield q was measured at room temperature from Quantaaurus-QY Plus C13534 (Hamamatsu) system consisting of a 150 W xenon lamp coupled to a monochromator, an integrating sphere, and two multichannel analyzers to record emission intensity. For each sample, the reported q values were based on the average values of three measurements with an accuracy of 10% .

The photon flux ($\text{photons}\cdot\text{s}^{-1}$), the radiant flux (W), and the luminous flux (lm) of the blue commercial chip and of the prototypes were measured with an integrating sphere ISP 150 L-131 (BaSO_4 coating, Instrument Systems) coupled to an array spectrometer MAS 40 (Instrument System). The number

of absorbed photons (N_A) corresponds to the difference between the number of photons emitted (N_e) by the bare blue commercial LED and those of the prototypes in the wavelength range 370–443 nm, taken the same time integration interval.

5. Theoretical section

Assuming that there are no interactions between the aCDs and $\text{Eu}(\text{tta})_3(\text{bpyO}_2)$ incorporated into the d-U(600) (this is justified by the fact that there are no superpositions between dU6-Eu and dU6-aCDs/Eu excitation/emission spectra, as already shown in Figure 2), it is possible to treat the dU6-Eu system separately using the procedures that start from the *in silico experiments* (computational simulations), passing through the IET and *levels population* analyses, until the theoretical *emission quantum yield* q (also called overall or external quantum yield Q_{Ln}^L).^[88]

In silico experiments: The DFT was employed to obtain the structure of dU6-Eu, as well as the isolated $\text{Eu}(\text{tta})_3(\text{bpyO}_2)$ complex. The structure of $\text{Eu}(\text{tta})_3(\text{bpyO}_2)$ was necessary to calculate the excited states of the complex. This was done using the TD-DFT to localize the donor states (T_1 and S_1) in the $\text{Eu}(\text{tta})_3(\text{bpyO}_2)$ complex and know how they can also interact with the d-U(600) states in dU6-Eu. All these procedures were performed within the same level of theory: B3LYP functional,^[89,90] Pople's basis set 6-31G(d)^[91] for O, H, C, N, F, and S atoms, and the MWB52 (pseudo-potential for the core electrons and basis set for the valence ones) for the Eu^{3+} ion.^[92]

Intramolecular energy transfer (IET): The IET rates were calculated based on the theory in literature.^[79,93,94] and described in details in the Supporting Information. Besides the energy transfer from the states of the ligands (S_1 and T_1) and the intrinsic emitting centers of the di-ureasil (triplet states $T_{(\text{NH})}$ and $T_{(\text{Si})}$ localized at the NH/C=O and $\text{O-O-Si}\equiv(\text{CO})_2$ groups, respectively) to the Eu^{3+} ion, this analysis also consists of the energy interchanged amongst the ligands and the triplet states of the di-ureasil hybrid moieties.

For the IET to the Eu^{3+} ion, the dipole-dipole (W_{d-d} , Equation S12), dipole-multipole (W_{d-m} , Equation S13), and exchange (W_{ex} , Equation S14) mechanisms were considered, whereas, for the Ligand-

to-Hybrid energy transfer, the dipole-dipole (W_{d-d}^{HL} , Equation S8) and exchange (W_{ex}^{HL} , Equation S7) mechanisms were used, these two are based on Förster-Dexter type expressions.

Levels population: The population analysis includes the kinetics between absorption rates, IET (both forward and backward processes), radiative and non-radiative decay rates of all parts involved (d-U(600), ligands, and the Eu^{3+} ion). This kinetics is described by an appropriate set of ODEs. This system of equations can be solved in the steady-state regime (when all derivatives are equals zero) or can be numerically solved by an interactive method.^[94] In the case of the dU6-Eu, we constructed a 7-level system of rate equations based on the energy level diagram (see Figure 4 and Equation S18 to S24, Supporting Information). The system of ODEs was solved using a numerical approach through the Radau method^[94] with a step-size of 5×10^{-6} s and a total number of 1,000 steps, resulting in simulations from 0 to 5 ms.

Supporting Information

Supporting Information is available from the Wiley Online Library or from the author.

Acknowledgements

This work was developed within the scope of the projects CICECO-Aveiro Institute of Materials, UIDB/50011/2020 & UIDP/50011/2020, and WINLEDs (POCI-01-0145-FEDER-030351), financed by *national funds* through the Portuguese Foundation for Science and Technology/MCTES. This work was also supported by the China Scholarship Council, grant: 201707920002 (2017–2020). A.N.C.N. also thanks to the NanoTBTech FET Open project (grant agreement no. 801305) for his postdoctoral fellowships.

Received: ((will be filled in by the editorial staff))

Revised: ((will be filled in by the editorial staff))

Published online: ((will be filled in by the editorial staff))

References

- [1] J. Zhou, J. L. Leão, Z. Liu, D. Jin, K. Wong, R. Liu, J.-C. G. Bünzli, *Small* **2018**, *14*, 1801882.
- [2] M. A. Hernández-Rodríguez, C. D. S. Brites, G. Antorrena, R. Piñol, R. Cases, L. Pérez-García, M. Rodrigues, J. A. Plaza, N. Torras, I. Díez, A. Millán, L. D. Carlos, *Adv. Opt. Mater.* **2020**, *8*, 2000312.
- [3] J. Long, M. S. Ivanov, V. A. Khomchenko, E. Mamontova, J.-M. Thibaud, J. Rouquette, M. Beaudhuin, D. Granier, R. A. S. Ferreira, L. D. Carlos, B. Donnadieu, M. S. C. Henriques, J. A. Paixão, Y. Guari, J. Larionova, *Science* **2020**, *367*, 671.
- [4] M. A. Cardoso, S. F. H. Correia, A. R. Frias, H. M. R. Gonçalves, R. F. P. Pereira, S. C. Nunes, M. Armand, P. S. André, V. de Zea Bermudez, R. A. S. Ferreira, *J. Rare Earths* **2020**, *38*, 531.
- [5] X. Ou, X. Qin, B. Huang, J. Zan, Q. Wu, Z. Hong, L. Xie, H. Bian, Z. Yi, X. Chen, Y. Wu, X. Song, J. Li, Q. Chen, H. Yang, X. Liu, *Nature* **2021**, *590*, 410.
- [6] A. N. Carneiro Neto, O. L. Malta, *Nature* **2021**, *590*, 396.
- [7] J. F. C. B. Ramalho, S. F. H. Correia, L. Fu, L. M. S. Dias, P. Adão, P. Mateus, R. A. S. Ferreira, P. S. André, *npj Flex. Electron.* **2020**, *4*, 11.
- [8] J. F. C. B. Ramalho, S. F. H. Correia, L. Fu, L. L. F. António, C. D. S. Brites, P. S. André, R. A. S. Ferreira, L. D. Carlos, *Adv. Sci.* **2019**, *6*, 1900950.
- [9] C. D. S. Brites, S. Balabhadra, L. D. Carlos, *Adv. Opt. Mater.* **2019**, *7*, 1801239.
- [10] K. Bando, K. Sakano, Y. Noguchi, Y. Shimizu, *J. Light Vis. Environ.* **1998**, *22*, 2.
- [11] X. Bai, G. Caputo, Z. Hao, V. T. Freitas, J. Zhang, R. L. Longo, O. L. Malta, R. A. S. Ferreira, N. Pinna, *Nat. Commun.* **2014**, *5*, 5702.
- [12] M. Shang, C. Li, J. Lin, *Chem. Soc. Rev.* **2014**, *43*, 1372.
- [13] L. D. Carlos, R. A. S. Ferreira, V. de Z. Bermudez, S. J. L. Ribeiro, *Adv. Mater.* **2009**, *21*, 509.
- [14] S. Parola, B. Julián-López, L. D. Carlos, C. Sanchez, *Adv. Funct. Mater.* **2016**, *26*, 6506.
- [15] Y. Tang, H. Wu, W. Cao, Y. Cui, G. Qian, *Adv. Opt. Mater.* **2020**, 2001817.
- [16] J. Manzur, R. C. De Santana, L. J. Q. Maia, A. Vega, E. Spodine, *Inorg. Chem.* **2019**, *58*, 10012.
- [17] Y. Wang, S. H. Xing, F. Y. Bai, Y. H. Xing, L. X. Sun, *Inorg. Chem.* **2018**, *57*, 12850.
- [18] X. Feng, Y. Feng, N. Guo, Y. Sun, T. Zhang, L. Ma, L. Wang, *Inorg. Chem.* **2017**, *56*, 1713.
- [19] Y. Yang, L. Chen, F. Jiang, M. Yu, X. Wan, B. Zhang, M. Hong, *J. Mater. Chem. C* **2017**, *5*, 1981.
- [20] H. Ji, X. Li, D. Xu, Y. Zhou, L. Zhang, Z. Zuhra, S. Yang, *Inorg. Chem.* **2017**, *56*, 156.
- [21] M. Fang, L. Fu, R. Ferreira, L. Carlos, *Materials* **2018**, *11*, 2246.
- [22] B. Yan, *RSC Adv.* **2012**, *2*, 9304.
- [23] J. Feng, H. Zhang, *Chem. Soc. Rev.* **2013**, *42*, 387.
- [24] V. de Zea Bermudez, L. D. Carlos, L. Alcácer, *Chem. Mater.* **1999**, *11*, 569.
- [25] V. T. Freitas, P. P. Lima, V. de Zea Bermudez, R. A. S. Ferreira, L. D. Carlos, *Eur. J. Inorg. Chem.* **2012**, *2012*, 5390.
- [26] R. A. S. Ferreira, C. D. S. Brites, C. M. S. Vicente, P. P. Lima, A. R. N. Bastos, P. G. Marques, M. Hiltunen, L. D. Carlos, P. S. André, *Laser Photon. Rev.* **2013**, *7*, 1027.
- [27] M. Fang, A. G. Bispo-Jr, L. Fu, R. A. S. Ferreira, L. D. Carlos, *J. Lumin.* **2020**, *219*, 116910.
- [28] H. Zhang, X. Shan, L. Zhou, P. Lin, R. Li, E. Ma, X. Guo, S. Du, *J. Mater. Chem. C* **2013**, *1*, 888.
- [29] N. Willis-Fox, M. Kraft, J. Arlt, U. Scherf, R. C. Evans, *Adv. Funct. Mater.* **2016**, *26*, 532.
- [30] P. Sutar, T. K. Maji, *Inorg. Chem.* **2017**, *56*, 9417.
- [31] C. D. S. Brites, P. P. Lima, N. J. O. Silva, A. Millán, V. S. Amaral, F. Palacio, L. D. Carlos, *Nanoscale* **2013**, *5*, 7572.
- [32] E. Ferreira Molina, N. A. Martins de Jesus, S. Paofai, P. Hammer, M. Amela-Cortes, M. Robin, S. Cordier, Y. Molard, *Chem. - A Eur. J.* **2019**, *25*, 15248.
- [33] M. Fang, L. Fu, S. Correia, R. Ferreira, L. Carlos, *Polymers* **2018**, *10*, 434.
- [34] L. D. Carlos, V. de Zea Bermudez, R. A. Sá Ferreira, L. Marques, M. Assunção, *Chem. Mater.* **1999**, *11*, 581.
- [35] A. Bastos, B. McKenna, M. Lima, P. S. André, L. D. Carlos, R. C. Evans, R. A. S. Ferreira, *ACS Omega* **2018**, *3*, 13772.
- [36] C. Hu, M. Li, J. Qiu, Y.-P. Sun, *Chem. Soc. Rev.* **2019**, *48*, 2315.
- [37] Z. Wang, Y. Liu, S. Zhen, X. Li, W. Zhang, X. Sun, B. Xu, X. Wang, Z. Gao, X. Meng, *Adv. Sci.* **2020**, *7*, 1902688.
- [38] B. Zhao, Z. Tan, *Adv. Sci.* **2021**, *8*, 2001977.
- [39] L. Wang, W. Li, L. Yin, Y. Liu, H. Guo, J. Lai, Y. Han, G. Li, M. Li, J. Zhang, R. Vajtai, P. M. Ajayan, M.

Wu, *Sci. Adv.* **2020**, *6*, eabb6772.

- [40] Z. Zhu, Y. Zhai, Z. Li, P. Zhu, S. Mao, C. Zhu, D. Du, L. A. Belfiore, J. Tang, Y. Lin, *Mater. Today* **2019**, *30*, 52.
- [41] H. Jia, Z. Wang, T. Yuan, F. Yuan, X. Li, Y. Li, Z. Tan, L. Fan, S. Yang, *Adv. Sci.* **2019**, *6*, 1900397.
- [42] B. Yuan, Z. Xie, P. Chen, S. Zhou, *J. Mater. Chem. C* **2018**, *6*, 5957.
- [43] S. Ghosh, C. Pal, S. Paul, M. Saha, D. Barman, S. K. De, *Chem. Commun.* **2018**, *54*, 14124.
- [44] D. Wang, W. U. Khan, Y. Wang, *Chem. – An Asian J.* **2019**, *14*, 286.
- [45] D. Wang, W. U. Khan, Z. Tang, Y. Wang, *Chem. – An Asian J.* **2018**, *13*, 292.
- [46] S. Wang, Z. Zhu, Y. Chang, H. Wang, N. Yuan, G. Li, D. Yu, Y. Jiang, *Nanotechnology* **2016**, *27*, 295202.
- [47] Y. Chen, B. Lei, M. Zheng, H. Zhang, J. Zhuang, Y. Liu, *Nanoscale* **2015**, *7*, 20142.
- [48] X.-F. Wang, G.-G. Wang, J.-B. Li, Z. Liu, W.-F. Zhao, J.-C. Han, *Chem. Eng. J.* **2018**, *336*, 406.
- [49] E. E. S. Teotonio, H. F. Brito, M. C. F. C. Felinto, C. A. Kodaira, O. L. Malta, *J. Coord. Chem.* **2003**, *56*, 913.
- [50] F. M. Cabral, D. A. Gállico, I. O. Mazali, F. A. Sigoli, *Inorg. Chem. Commun.* **2018**, *98*, 29.
- [51] R. Ilmi, S. Anjum, A. Haque, M. S. Khan, *J. Photochem. Photobiol. A Chem.* **2019**, *383*, 111968.
- [52] S. M. Borisov, O. S. Wolfbeis, *Anal. Chem.* **2006**, *78*, 5094.
- [53] G. B. V. Lima, J. C. Bueno, A. F. da Silva, A. N. Carneiro Neto, R. T. Moura, E. E. S. Teotonio, O. L. Malta, W. M. Faustino, *J. Lumin.* **2020**, *219*, 116884.
- [54] B. Chen, J. Feng, *J. Phys. Chem. C* **2015**, *119*, 7865.
- [55] B. Dai, D. Deng, H. Yu, L. Lei, Y. Li, C. Li, S. Xu, *RSC Adv.* **2016**, *6*, 72149.
- [56] Z. Abbas, S. Dasari, A. K. Patra, *RSC Adv.* **2017**, *7*, 44272.
- [57] M. E. De Mesquita, S. A. Júnior, F. R. G. E Silva, M. A. Couto Dos Santos, R. O. Freire, N. B. C. Júnior, G. F. De Sá, *J. Alloys Compd.* **2004**, *374*, 320.
- [58] Z. Shen, D. Xu, N. Cheng, X. Zhou, X. Chen, Y. Xu, Q. He, *J. Coord. Chem.* **2011**, *64*, 2342.
- [59] B. Francis, M. M. Nolasco, P. Brandão, R. A. S. Ferreira, R. S. Carvalho, M. Cremona, L. D. Carlos, *Eur. J. Inorg. Chem.* **2020**, *2020*, 1260.
- [60] X. Miao, D. Qu, D. Yang, B. Nie, Y. Zhao, H. Fan, Z. Sun, *Adv. Mater.* **2018**, *30*, 1704740.
- [61] S. A. Brandán, L. C. Bichara, H. E. Lans, E. G. Ferrer, M. B. Gramajo, *Adv. Phys. Chem.* **2011**, *2011*, 1.
- [62] C. Djordjevic, M. Lee, E. Sinn, *Inorg. Chem.* **1989**, *28*, 719.
- [63] P. Tarakeshwar, S. Manogaran, *Spectrochim. Acta Part A Mol. Spectrosc.* **1994**, *50*, 2327.
- [64] Y. Mido, *Spectrochim. Acta Part A Mol. Spectrosc.* **1972**, *28*, 1503.
- [65] Y. Gao, Y. Jiao, W. Lu, Y. Liu, H. Han, X. Gong, M. Xian, S. Shuang, C. Dong, *J. Mater. Chem. B* **2018**, *6*, 6099.
- [66] E. Shuang, Q. X. Mao, X. L. Yuan, X. L. Kong, X. W. Chen, J. H. Wang, *Nanoscale* **2018**, *10*, 12788.
- [67] Z. Sun, X. Li, Y. Wu, C. Wei, H. Zeng, *New J. Chem.* **2018**, *42*, 4603.
- [68] Y. Zhang, Y. H. He, P. P. Cui, X. T. Feng, L. Chen, Y. Z. Yang, X. G. Liu, *RSC Adv.* **2015**, *5*, 40393.
- [69] J. Schneider, C. J. Reckmeier, Y. Xiong, M. von Seckendorff, A. S. Sussha, P. Kasák, A. L. Rogach, *J. Phys. Chem. C* **2017**, *121*, 2014.
- [70] W. Wang, B. Wang, H. Embrechts, C. Damm, A. Cadranet, V. Strauss, M. Distaso, V. Hinterberger, D. M. Guldi, W. Peukert, *RSC Adv.* **2017**, *7*, 24771.
- [71] S. Qu, X. Wang, Q. Lu, X. Liu, L. Wang, *Angew. Chemie Int. Ed.* **2012**, *51*, 12215.
- [72] L. Sciortino, A. Sciortino, R. Popescu, R. Schneider, D. Gerthsen, S. Agnello, M. Cannas, F. Messina, *J. Phys. Chem. C* **2018**, *122*, 19897.
- [73] B. E. Warren, *X-ray Diffraction*, 1st ed., Dover Publications, Inc., New York, **1990**.
- [74] A. Guinier, *X-ray Diffraction in Crystals, Imperfect Crystals, and Amorphous Bodies*, Dover Publications, Inc., New York, **1994**.
- [75] V. de Zea Bermudez, R. A. Sá Ferreira, L. D. Carlos, C. Molina, K. Dahmouche, S. J. L. Ribeiro, *J. Phys. Chem. B* **2001**, *105*, 3378.
- [76] M. Fernandes, V. De Zea Bermudez, R. A. Sá Ferreira, L. D. Carlos, A. Charas, J. Morgado, M. M. Silva, M. J. Smith, *Chem. Mater.* **2007**, *19*, 3892.
- [77] J. Zhu, X. Bai, Y. Zhai, X. Chen, Y. Zhu, G. Pan, H. Zhang, B. Dong, H. Song, *J. Mater. Chem. C* **2017**, *5*, 11416.
- [78] Y. Wang, S. Kalytchuk, L. Wang, O. Zhovtiuk, K. Cepe, R. Zboril, A. L. Rogach, *Chem. Commun.* **2015**, *51*, 2950.
- [79] P. P. Lima, S. S. Nobre, R. O. Freire, S. A. Júnior, R. A. Sá Ferreira, U. Pischel, O. L. Malta, L. D. Carlos, *J.*

Phys. Chem. C **2007**, *111*, 17627.

- [80] C. M. S. Vicente, L. Fu, P. S. André, V. de Zea Bermudez, R. A. S. Ferreira, *Opt. Quantum Electron.* **2016**, *48*, 389.
- [81] A. Katelnikovas, H. Bettentrup, D. Uhlich, S. Sakirzanovas, T. Jüstel, A. Kareiva, *J. Lumin.* **2009**, *129*, 1356.
- [82] Z. Wang, X. Zhao, Z. Guo, P. Miao, X. Gong, *Org. Electron.* **2018**, *62*, 284.
- [83] T. Zhang, F. Zhao, L. Li, B. Qi, D. Zhu, J. Lü, C. Lü, *ACS Appl. Mater. Interfaces* **2018**, *10*, 19796.
- [84] C. Wang, T. Hu, Y. Chen, Y. Xu, Q. Song, *ACS Appl. Mater. Interfaces* **2019**, *11*, 22332.
- [85] X. F. Wang, G. G. Wang, J. B. Li, Z. Liu, Y. X. Chen, L. F. Liu, J. C. Han, *Chem. Eng. J.* **2019**, *361*, 773.
- [86] L. Wang, Q. Ou, Q. Peng, Z. Shuai, *J. Phys. Chem. A* **2021**, *125*, 1468.
- [87] N. D. Q. Anh, P. X. Le, H.-Y. Lee, *Curr. Opt. Photonics* **2019**, *3*, 78.
- [88] L. E. do N. Aquino, G. A. Barbosa, J. de L. Ramos, S. O K Giese, F. S. Santana, D. L. Hughes, G. G. Nunes, L. Fu, M. Fang, G. Poneti, A. N. Carneiro Neto, R. T. Moura, R. A. S. Ferreira, L. D. Carlos, A. G. Macedo, J. F. Soares, *Inorg. Chem.* **2021**, *60*, 892.
- [89] C. Lee, W. Yang, R. G. Parr, *Phys. Rev. B* **1988**, *37*, 785.
- [90] A. D. Becke, *J. Chem. Phys.* **1993**, *98*, 5648.
- [91] W. J. Hehre, W. A. Lathan, *J. Chem. Phys.* **1972**, *56*, 5255.
- [92] M. Dolg, H. Preuss, *J. Chem. Phys.* **1989**, *90*, 1730.
- [93] O. L. Malta, *J. Lumin.* **1997**, *71*, 229.
- [94] A. N. Carneiro Neto, E. E. S. Teotonio, G. F. de Sá, H. F. Brito, J. Legendziewicz, L. D. Carlos, M. C. F. C. Felinto, P. Gawryszewska, R. T. Moura Jr., R. L. Longo, W. M. Faustino, O. L. Malta, In *Handbook on the Physics and Chemistry of Rare Earths, volume 56* (Eds.: Bünzli, J.-C. G.; Pecharsky, V. K.), Elsevier, **2019**, pp. 55–162.